

# Thermal ageing of Pt on low-surface-area $\text{CeO}_2\text{--ZrO}_2\text{--La}_2\text{O}_3$ mixed oxides: Effect on the OSC performance

Jun Fan, Xiaodong Wu, Xiaodi Wu, Qing Liang, Rui Ran, Duan Weng<sup>\*</sup>

*Laboratory of Advanced Materials, Department of Materials Science and Engineering, Tsinghua University, Beijing 100084, China*

Received 21 May 2007; received in revised form 23 November 2007; accepted 24 November 2007

Available online 16 January 2008

## Abstract

This work aims at exploring the thermal ageing mechanism of Pt on ceria-based mixed oxides and the corresponding effect on the oxygen storage capacity (OSC) performance of the support material. Pt was supported on low-surface-area  $\text{CeO}_2\text{--ZrO}_2\text{--La}_2\text{O}_3$  mixed oxides (CK) by impregnation method and subsequently calcined in static air at 500, 700 and 900 °C, respectively. The evolutions of textural, microstructural and redox properties of catalysts after the thermal treatments were identified by means of X-ray diffraction (XRD), Raman, X-ray photoelectron spectroscopy (XPS), temperature programmed reduction (TPR) and high-resolution transmission electron microscope (HRTEM). The results reveal that, besides the sintering of Pt, encapsulation of metal by the mixed oxides occurs at the calcination temperature of 700 °C and above. The burial of Pt crystallites by support particles is proposed as a potential mechanism for the encapsulation. Further, the HRTEM images show that the distortion of the mixed oxides lattice and other crystal defects are distributed at the metal/oxides interface, probably indicating the interdiffusion/interaction between the metal and mixed oxide. In this way, encapsulation of Pt is capable to promote the formation of  $\text{Ce}^{3+}$  or oxygen vacancy on the surface and in the bulk of support. The OSC results show that the reducibility and oxygen release behavior of catalysts are related to both the metal dispersion and metal/oxides interface, and the latter seems to be more crucial for those supported on low-surface-area mixed oxides. Judging by the dynamic oxygen storage capacity (DOSC), oxygen storage capacity complete (OSCC) and oxygen releasing rate, the catalyst calcined at 700 °C shows the best OSC performance. This evident promotion of OSC performance is believed to benefit from the partial encapsulation of Pt species, which leads to the increment of  $\text{Ce}^{3+}$  or oxygen vacancies both on the surface and in the bulk of oxides despite a loss of chemisorption sites on the surface of metal particles.

© 2007 Elsevier B.V. All rights reserved.

**Keywords:** Pt;  $\text{CeO}_2\text{--ZrO}_2\text{--La}_2\text{O}_3$  mixed oxides; Ageing; Encapsulation; OSC

## 1. Introduction

$\text{CeO}_2\text{--ZrO}_2$  mixed oxides have drawn great attention for the outstanding oxygen storage capacity (OSC) [1–5]. Many studies have been directed to explore the factors, such as composition [6], phase structure [7–9] and atomic arrangement in crystal lattice [10,11], that affect the OSC performance of  $\text{CeO}_2\text{--ZrO}_2$  mixed oxides. Considering the effect of strong metal–support interaction (SMSI) between reducible ceria and supported noble metal, some studies have been focused on the influence of loaded metal on the redox and OSC performance of catalysts, with ceria and ceria-based oxides serving as supports.

Hori et al. [12] believed that the properties of oxygen storage material (OSM) but not the interactions with Pt were the dominant factors that made  $\text{CeO}_2\text{--ZrO}_2$  mixed oxides a better OSM than  $\text{CeO}_2$ . However, according to Bozo et al. [13], the presence of Pt or Pd enhanced the number of oxygen vacancies, which appeared to be the key point of high oxygen activation and mobility, by lowering the effective activation energy for the formation of oxygen vacancies in  $\text{Ce}_{0.67}\text{Zr}_{0.33}\text{O}_2$  mixed oxides. Arena et al. [14] investigated the oxidation of CO over 1%Pt/ $\text{Ce}_{0.6}\text{Zr}_{0.4}\text{O}_2$  in the absence of gaseous oxygen by transient reactivity tests, and the results highlighted the role of Pt/support interface in providing oxygen reactive sites. Up to now, to explore the influence of metal on the OSC performance of the supported catalysts is still of great challenge. That is because the detailed procedure of oxygen release from  $\text{CeO}_2$ -based mixed oxides with the participation of metal remains

<sup>\*</sup> Corresponding author. Tel.: +86 10 62772726; fax: +86 10 62772726.

E-mail address: [duanweng@tsinghua.edu.cn](mailto:duanweng@tsinghua.edu.cn) (D. Weng).

ambiguous although various models [15,16] have been constructed to describe correlated oxygen diffusion and interaction steps.

It is well known that the exposure of catalysts to high temperatures will induce the agglomeration and sintering of noble metal, lowering the overall active surface area available for the conversion of pollutants [17,18]. Specifically, early research reported that, due to the sintering of Pt particles, the activity of Pt/Al<sub>2</sub>O<sub>3</sub> catalysts decreased significantly after thermal ageing in an oxidative atmosphere compared with that in a reductive one [19,20]. However, Nagai et al. [21] reported that for a Pt catalyst supported by ceria, the Pt–O–Ce bond formed by the Pt-oxide–support interaction acted as an anchor and inhibited the sintering of Pt particles under oxidizing condition at high temperature. Another mechanism of noble metal ageing was depicted as the deep encapsulation of metal by support material, which is induced by the collapse of the support. Graham et al. [22] reported an example of this phenomenon, in which about one-quarter of the 2.25 wt.% Pd loaded onto high-surface-area Ce<sub>0.5</sub>Zr<sub>0.5</sub>O<sub>2</sub> was effectively lost on a redox ageing at 1050 °C, and later they confirmed the encapsulation of Rh by CeO<sub>2</sub>–ZrO<sub>2</sub> mixed oxides [23]. These studies made it clear that the synergetic effect of many factors, such as the nature of noble metal, the textural and chemical properties of support and the ageing conditions, maintains the complexity of the metal ageing mechanism.

This work deals with a combined investigation of thermal ageing of Pt on a low-surface-area ceria-based mixed oxides and corresponding effects on the OSC performance of the support. La<sup>3+</sup> cations were doped into CeO<sub>2</sub>–ZrO<sub>2</sub> mixed oxides to impede the segregation of Ce- and Zr-rich phases occurring at high temperature [24] and Pt was loaded by impregnation and sequential calcinations at different temperatures. The thermal ageing mechanism of Pt on low-surface-area CeO<sub>2</sub>–ZrO<sub>2</sub>–La<sub>2</sub>O<sub>3</sub> mixed oxides (CK) was investigated by analyzing the variations of textural, structural and redox properties of the catalysts as well as the status of metal/oxide interface after calcinations. Furthermore, with the interaction between metal and oxides being considered, the effect of thermal ageing of Pt on the OSC performance of catalysts was analyzed.

## 2. Experimental

### 2.1. Catalyst preparation

CeO<sub>2</sub>–ZrO<sub>2</sub>–La<sub>2</sub>O<sub>3</sub> mixed oxides were synthesized by citric-aided sol–gel method. The nitrates Ce(NO<sub>3</sub>)<sub>3</sub>·6H<sub>2</sub>O, ZrO(NO<sub>3</sub>)<sub>2</sub>·5H<sub>2</sub>O and La(NO<sub>3</sub>)<sub>3</sub>·6H<sub>2</sub>O were mixed according to the molar ratio of Ce:Zr = 67:33 and the weight content of La = 2%. Citric acid was used as the complexing agent. Appropriate glycol was added as the dispersant followed by evaporation and peptization. The sol was heated at 100 °C until a spongy yellow gel remained. Then the gel was submitted to decomposition at 300 °C for 1 h and calcination at 500 °C for 3 h to form CeO<sub>2</sub>–ZrO<sub>2</sub>–La<sub>2</sub>O<sub>3</sub> mixed oxides. The as-prepared powders were further heated up to 1050 °C at the rate of

6 °C min<sup>−1</sup> in static air and preserved at that temperature for 6 h. After cooling to room temperature in the furnace, the so-called CK support with low surface area was obtained. Pt was loaded by impregnating CK powders in the aqueous solution of H<sub>2</sub>PtCl<sub>6</sub>. The nominal weight content of Pt is 2%. The impregnated CK powders were then divided into three shares and calcined at 500, 700 and 900 °C in static air for 3 h to gain a series of catalysts named as P5CK, P7CK and P9CK, respectively.

### 2.2. Characterization

The specific surface area was determined by Brunauer–Emmett–Teller (BET) method with a Quantachrome NOVA instrument using Ar as carrier and N<sub>2</sub> as adsorbent. The powder X-ray diffraction (XRD) patterns were collected on a Japan Rigaku D/max-RB diffractometer employing Cu Kα radiation ( $\lambda = 1.5418 \text{ \AA}$ ). The X-ray tube was operated at 40 kV and 120 mA. The continuous scan was performed at 0.02° intervals in the range of  $20^\circ \leq 2\theta \leq 80^\circ$  with scanning velocity of 2° min<sup>−1</sup>. The crystal phase was identified with the help of the JCPDS cards. A particular observation of Pt (2 0 0) peak was obtained by step scan at 0.01° intervals. The calculations and analyses based on the XRD data were assisted by the THX application software. The lattice parameters were calculated with the application of least-squares refinement of cell dimensions from powder data by Cohen's method. The average crystallite size of the mixed oxides was estimated according to Debye–Scherrer equation [8].

Raman spectra were acquired with a Renishaw RM 2000 microscopic confocal Raman spectrometer. The emission line at 632.8 nm from a He–Ne laser was focused on the samples (analyzing spot diameter of 5 μm) under microscope. The power of the incident beam on samples was 4.7 mW and the scattered radiation was collected at 180° with the resolution of 1 cm<sup>−1</sup>.

The X-ray photoelectron spectroscopy (XPS) experiments were carried out on a PHI-Quantera SXM system equipped with a monochromatic Al Kα X-rays under ultra-high vacuum ( $6.7 \times 10^{-8} \text{ Pa}$ ). A 100 μm spot size was used for analysis. Sample charging during the measurement was compensated by an electron flood gun. The electron takeoff angle was 45° with respect to the sample surface. The XPS data from the regions related to the C 1s, O 1s, Cl 2p, Zr 3d, La 3d, Ce 3d and Pt 4f core levels were recorded for each sample. The binding energies were calibrated internally by the carbon deposit C 1s binding energy (BE) at 284.8 eV.

High-resolution transmission micrographs were shot by a JEOL 2011 electron microscopy, operating at 200 kV. Before the observations, the powder samples were diluted in ethanol and dispersed by ultrasonic. Afterward, a drop of each solution was deposited on a Cu grid coated by a holed carbon film and dried in air. Images with scales of 20, 10, 5 and 2 nm were collected. The size of each observed metal particle was measured. The Pt dispersion ( $D_{\text{Pt}}$ ) was calculated based on the measured particle sizes using the formula and constants reported in literature [25] and the average particle size ( $d_{\text{Pt}}$ ) was

Table 1  
Structural and textural properties of CeO<sub>2</sub>–ZrO<sub>2</sub>–La<sub>2</sub>O<sub>3</sub> mixed oxides and the Pt-supported samples

| Samples | Surface area (m <sup>2</sup> g <sup>−1</sup> ) | Oxide crystallite size (nm) | Lattice parameter (Å) | Pt dispersion (%) <sup>a</sup> | Pt particle size (nm) <sup>b</sup> |
|---------|--|-----------------------------|-----------------------|--------------------------------|------------------------------------|
| CK      | 4.3  | 26.4 ± 0.6                  | 5.3408 ± 0.0004       | –                              | –                                  |
| P5CK    | 4.2  | 26.1 ± 0.7                  | 5.3413 ± 0.0005       | 23                             | 4.9                                |
| P7CK    | 5.5  | 26.0 ± 0.7                  | 5.3495 ± 0.0006       | 18                             | 6.2                                |
| P9CK    | 5.3  | 26.6 ± 1.1                  | 5.3465 ± 0.0006       | 10                             | 11.2                               |

<sup>a</sup> Derived from HRTEM images and calculated with the assistance of the formula and constants reported in [25].

<sup>b</sup> Estimated from HRTEM images.

calculated with the formula  $d_{\text{Pt}}$  (nm) = 1.1/ $D_{\text{Pt}}$  as presented in literature [26]. Image analysis was performed on digitized images using Digital Micrograph 3.5.2. Digital diffraction patterns (DDPs) corresponded to the log-scaled power spectrum of the corresponding fast Fourier transformations (FFTs).

With the aim of characterizing the redox properties of the CK support and Pt-loaded catalysts, temperature programmed reduction (TPR) was performed in a microreactor, and the signals of H<sub>2</sub> uptake were collected by a thermal conductivity detector (TCD). Before each measurement, about 100 mg sample was first pretreated in pure N<sub>2</sub> (40 ml min<sup>−1</sup>) at 300 °C for 1 h followed by cooling down to room temperature in the same atmosphere. The flow of 5% H<sub>2</sub>/N<sub>2</sub> (40 ml min<sup>−1</sup>) was then introduced as reducing agent and the sample was heated up to 750 °C from room temperature at the rate of 10 °C min<sup>−1</sup>.

### 2.3. OSC measurements

OSC measurement was conducted based on the method proposed by Yao and Yu Yao [27]. The reactants used in the measurement were 4% CO/(1% Ar + He) and 2% O<sub>2</sub>/(1% Ar + He). The titrating gas flows were regulated by mass flow controllers. The mass spectrometer was used to monitor the concentration of He ( $m/e$  = 4), CO ( $m/e$  = 28), O<sub>2</sub> ( $m/e$  = 32), Ar ( $m/e$  = 40) and CO<sub>2</sub> ( $m/e$  = 44) in outlet gas flow at 0.1 s intervals during each experiment. OSC was quantified in terms of micromole of CO<sub>2</sub> per gram of catalyst (μmol CO<sub>2</sub> g<sup>−1</sup>) by integrating the concentration of CO<sub>2</sub> in outlet gas pulses.

Two testing modes, dynamic mode and pulse mode, were applied to measure the so-called dynamic oxygen storage capacity (DOSC) and oxygen storage capacity complete (OSCC) of the catalysts, respectively. In dynamic mode, OSC measurement was operated at certain temperatures by alternately injecting CO/(Ar + He) and O<sub>2</sub>/(Ar + He) with duration of 5 s for each, which meant a test frequency of 0.1 Hz. The test temperatures range from 200 to 500 °C with intervals of 100 °C. Before the test at each temperature point, the samples (typically 25 mg) were oxidized in O<sub>2</sub>/(Ar + He) for 5 min and then purged by pure He for 5 min.

After the samples were oxidized in O<sub>2</sub>/(Ar + He) for 5 min at 500 °C, the pulse OSC measurement was operated at the same temperature to obtain the OSCC values. The test procedure consisted of the first ten 5-s long pulses of 4% CO/(1% Ar + He) with 40-s long outgassing of pure He between two adjoining CO pulses. The OSCC was quantified by integrating the

concentration of CO<sub>2</sub> produced in the ten pulses. The amount of the most reactive oxygen (labile oxygen) of the catalyst, denoted as LOSC, is quantified according to the amount of oxygen species that react during the first CO pulse.

## 3. Results and discussion

### 3.1. XRD and Raman studies

Due to the compact relationship between the bulk structure and the surface properties of CeO<sub>2</sub>-based mixed oxides, a detailed phase analysis is an indispensable step of micro-structural characterization. The structural and textural properties of the CK support and the Pt-supported catalysts are summarized in Table 1. The surface area and average crystallite size of the CK support show inconspicuous change after the impregnation and sequential thermal treatment for the deposition of H<sub>2</sub>PtCl<sub>6</sub>. This observation indicates that the thermal ageing over CK support at 1050 °C under oxidative condition is severe enough to raze the rough and porous surface of CeO<sub>2</sub>–ZrO<sub>2</sub>–La<sub>2</sub>O<sub>3</sub> mixed oxides.

The XRD patterns of all samples are shown in Fig. 1a. The symmetrical peaks of the support are consistent with the characteristic peaks of cubic CeO<sub>2</sub>, indicating the formation of CeO<sub>2</sub>–ZrO<sub>2</sub>–La<sub>2</sub>O<sub>3</sub> solid solutions. Beside those of the CK support, the characteristic peaks of metallic Pt are also observed over all the Pt-supported samples. It can be clearly seen from Fig. 1a that the intensity of Pt (1 1 1) peak follows the order of P5CK > P7CK > P9CK. Generally speaking, the higher diffraction angle the peak is located at, the more precise information can be collected from the diffraction profile. The step scans of Pt (2 0 0) peak are presented in Fig. 1b. It is worth noting that the (2 0 0) peak intensity of Pt also becomes weakened with the rise of calcination temperature. These observations seem to be conflictive with the normal understanding that Pt would suffer more severe sintering at higher temperature and accordingly present narrower and more intensified diffraction peaks [28]. One possible explanation can be elucidated as that higher temperature induces a disaggregation of Pt particles, which was called redispersion by some researchers [17,28]. In this work, the noble metal was aged in air and mild oxygen treatment has been reported to be insufficient to induce the redispersion of Pt in three-way catalysts (TWCs) [17]; on the other hand, the average Pt particle size presented in Table 1 keeps on increasing with the rise of calcination temperature, which to a large extent excludes the occurrence of redispersion. Therefore, we alternatively

attribute this abnormal decrease of diffraction peak intensity to the interaction between reducible ceria-based support and Pt crystallites. A similar phenomenon exists in the system of redox-aged Pd/CeO<sub>2</sub>-ZrO<sub>2</sub> catalysts [23,29]. The intensity of Pd (1 1 1) diffraction peak also decreased after the high-temperature ageing and the loss of peak intensity was attributed to the oxidation of Pd. Similarly, the loss of Pt diffraction peak intensity in this work arises from the oxidation of Pt by ceria at the metal/support interface. The produced Pt<sup>2+</sup>/Pt<sup>4+</sup> ions probably dissolve in the mixed oxides lattice, escaping from the detection of XRD technique [30]. Hence, the ordered arrangement of Pt atoms in metal lattice at the metal/oxides interface is interrupted by the metal–support interaction and consequently the diffraction of X-ray is weakened.

The variations in lattice parameters of the samples in Table 1 also indicate the occurrence of such a metal–support interaction. It is shown that the loading of metal introduces an increase of the oxide lattice parameters, especially for P7CK and P9CK. The separation of Ce- and Zr-rich phases and the increasing content of Ce<sup>3+</sup> associated with the formation of oxygen vacancies are both possibly responsible for the lattice expansion. Since the superior symmetry of diffraction peaks in Fig. 1 allows us to rule out the segregation of phases, the effect of metal loading on the concentration of oxygen vacancy or Ce<sup>3+</sup> is considered to be the dominant factor. It has been proved by the conductivity measurement that the presence of Pt and Pd is capable to increase the amount of oxygen vacancy in Ce<sub>0.67</sub>Zr<sub>0.33</sub>O<sub>2</sub> by lowering the effective activation energy for the formation of oxygen vacancies [13]. In our previous work [30], we observed that the incorporation of Pt<sup>2+</sup> or Pt<sup>4+</sup> into the lattice of Ce<sub>0.67</sub>Zr<sub>0.33</sub>O<sub>2</sub> resulted in an expansion of the oxides lattice although the ionic radii of Pt<sup>2+</sup> and Pt<sup>4+</sup> (0.80 and 0.63 Å, respectively) are smaller than those of Ce<sup>4+</sup> and Zr<sup>4+</sup> (0.97 and 0.84 Å, respectively). This phenomenon was explained from the point of view of the interaction between metal and mixed

oxides and was interpreted by the enhanced concentration of Ce<sup>3+</sup> (1.14 Å), which contributed mostly to the lattice expansion. Combined with the thermal-ageing-induced decrease of the Pt diffraction peak intensity, the increase of oxides lattice parameter may be explained by the dissolving of platinum species into the oxides lattice via the interdiffusion and the creation of oxygen vacancies or Ce<sup>3+</sup> in vicinity of metal/oxide interface by Pt/Ce interaction.

Since the X-ray pattern reflects the cation order–disorder and lattice distortion, and is poorly sensitive to oxygen sublattice, the nuances in the short range oxygen displacement of the solid solutions were examined by Raman spectroscopy, which is sensitive to both M–O bond arrangement and lattice defects. As shown in Fig. 2, no obvious shifts in the band position or variations of band width are noted. All samples maintain a cubic phase in respect that a prominent peak at 478 cm<sup>−1</sup>, owing to F<sub>2g</sub> Raman active mode of the fluorite-like structure, is observed. The broad band at ca. 1193 cm<sup>−1</sup> is generally assigned to the second order scattering [31]. The presence of the broad band at 618 cm<sup>−1</sup> is due to longitudinal optical (LO) mode of ceria which arises from the relaxation of symmetry rules as stated in literatures [32,33]. Generally, oxygen vacancies, originated from the substitution of zirconium into the ceria lattice with high temperature calcinations, are responsible for the emergence of this band. The appearance of weak bands at 305 and 126 cm<sup>−1</sup> can be attributed to the displacement of oxygen atoms from their ideal fluorite lattice positions [34,35]. Such a rearrangement of oxygen atoms means the transformation of cubic phase to a so-called pseudo-cubic *t'* phase, where cation sublattice remains cubic structure while oxygen atoms undergo a tetragonal distortion. All

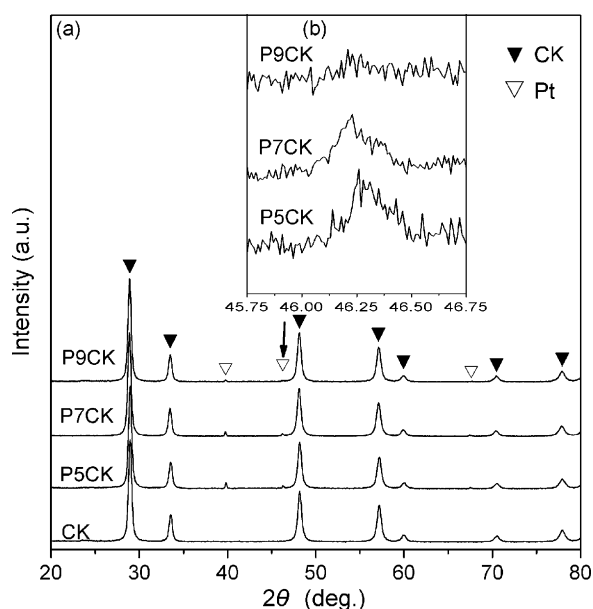


Fig. 1. XRD patterns of (a) CK support and Pt-loaded catalysts by continuous scan and (b) Pt (2 0 0) peak by step scan.

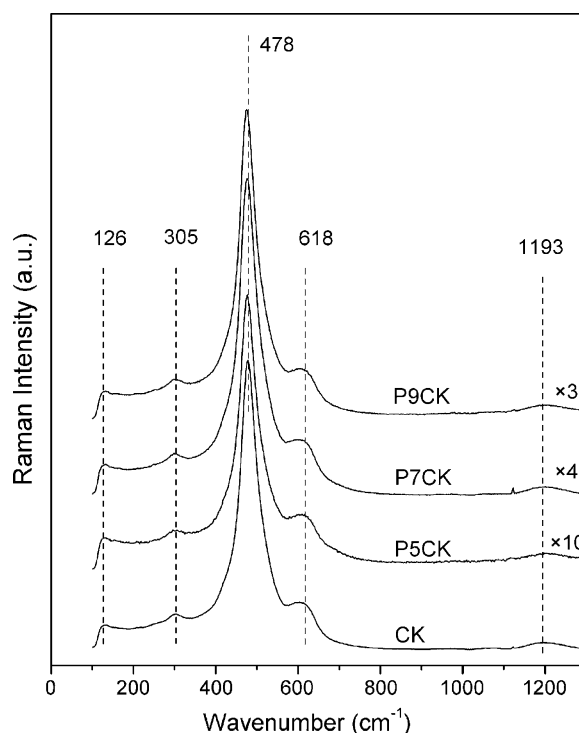


Fig. 2. Raman spectra of CK support and Pt-loaded catalysts.



samples present similar profiles. This observation suggests that after the oxidizing ageing at 1050 °C, the displacement of oxygen atoms in the sublattice is to some extent stable and the loading of metal and subsequential thermal ageing treatments at lower temperatures can hardly drive the further transformation of anionic sublattice.

### 3.2. XPS studies

An XPS investigation was conducted to provide information of the surface elemental distribution and the oxidation states of cerium and platinum. The Pt 4f spectra of all samples are shown in Fig. 3. The peaks located at 72.6–72.7 eV are attributed to  $\text{Pt}^{2+}$  4f<sub>7/2</sub> while the peaks at 70.7 eV are assigned to  $\text{Pt}^0$  4f<sub>7/2</sub>. A spin-orbit splitting of 3.35 eV, according with the literature [36], was fixed as a constraint in the fitting procedure of Pt peak positions. As shown in Fig. 4, the curves of Ce 3d spectra are composed of eight peaks corresponding to four pairs of spin-orbit doublets. The labeling of the peaks follows the convention [24]. Letters *u* and *v* refer to the 3d<sub>3/2</sub> and 3d<sub>5/2</sub> spin-orbit components, respectively. The spin-orbit splitting, in accordance with the literatures [14,15], is 18.4 eV. The peaks marked as *u* (900.6–901.0 eV), *u'* (907.5–907.7 eV) and *u'''* (916.6–916.9 eV) arise from  $\text{Ce}^{4+}$  3d<sub>3/2</sub> while the peaks labeled as *v* (882.2–882.6 eV), *v'* (889.1–889.3 eV) and *v'''* (898.2–898.5 eV) arise from  $\text{Ce}^{4+}$  3d<sub>5/2</sub>. The couples corresponding to one of the two possible electron configuration of the final state of the  $\text{Ce}^{3+}$  species are labeled as *u'* (903.5–904.2 eV) and *v'* (885.1–885.8 eV). The relative percentages of the platinum and cerium species are obtained by the area ratios of  $\text{Pt}^{2+}$  4f<sub>7/2</sub>/ $\text{Pt}^0$  4f<sub>7/2</sub> and  $\text{Ce}^{4+}$  3d<sub>5/2</sub> (*v*, *v'* and *v'''*)/ $\text{Ce}^{3+}$  3d<sub>5/2</sub> (*v'*), respectively. The surface elemental contents calculated from the normalized peak areas of the Ce 3d, Zr 3d, La 3d, Pt 4f and O 1s core level spectra and the relative concentrations of  $\text{Pt}^{2+}$  and  $\text{Ce}^{3+}$  for the metal-loaded samples are listed in Table 2.

The surface content of Pt element decreases significantly with the rise of calcination temperature after impregnation, which may arise from the sintering of Pt particles. It has presented a loss of Pt atoms exposed on the surface of metal particles by the decrease of the metal dispersion as listed in Table 1. However, in comparison to P5CK, the decline of metal dispersion is not severe enough to decrease the surface content of Pt species by as much as ca. 84% for P7CK, and the disappearance of Pt 4f spectrum of P9CK is even more unexpected in the case that the XRD pattern has declared the existence of Pt. Therefore, the encapsulation of Pt by the CK support should be taken into account. Partial metal particles on P7CK are believed to be encapsulated and nearly all Pt species on P9CK are shielded from the detection of XPS by mixed oxides. Since the detection depth of XRD extends more deeply into the particles than that of XPS, it is possible for XRD to detect the buried Pt particles in the bulk of mixed oxides while XPS reports a disappearance of Pt species on the surface. A similar encapsulation of Pd by low-surface-area ceria–zirconia supports was previously reported by Graham et al. [37].

As listed in Table 2, Pt species almost present in the form of PtO for P5CK. This observation seems to be inconsistent with

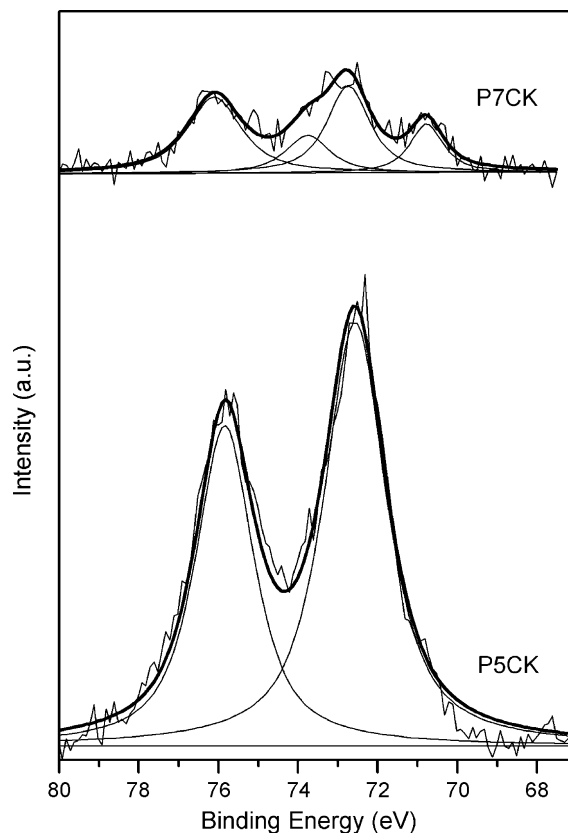


Fig. 3. Pt 4f spectra for the Pt-loaded catalysts.

the XRD results, which claim the presence of Pt metal instead of PtO. Still, a plausible explanation can be related to distinguishable detection depths of XRD and XPS. Based on our former research [38], it is suggested that after an oxidizing thermal treatment, Pt particles may be enveloped by platinum oxide layers, which are more easily detected by XPS than by XRD. As reported by many research groups [7,9], platinum oxide experiences a decomposition during high temperature calcination, which explains the decrease of relative content of  $\text{Pt}^{2+}$  in Pt from 100% for P5CK to 83% for P7CK by such a surface characterization technique.

Table 2 also shows the relative concentration of  $\text{Ce}^{3+}$  in Ce in the sequence of P7CK > P5CK > P9CK. As reported in literature [13] and the references therein, the presence of  $\text{Ce}^{3+}$  is associated with the formation of oxygen vacancies, which can exist under oxidizing conditions on account of the nanocrystalline nature of the support. It has been presented above that the content of  $\text{Ce}^{3+}$  or oxygen vacancy is the main factor that influences the lattice parameter in this work. Associated with the largest lattice parameter of P7CK, it is of great possibility that the concentration of  $\text{Ce}^{3+}$  in P7CK, both on the surface and in the bulk, is the highest among all catalysts. Therefore, both the metal encapsulated in the bulk of oxides and the residual metals dispersed on the surface seem to facilitate the reduction of  $\text{Ce}^{4+} \rightarrow \text{Ce}^{3+}$  or oxygen vacancy formation. In the case of P9CK, the lowest relative concentration of  $\text{Ce}^{3+}$  on the surface accompanies with the absence of surface Pt. Based on the above fact and the second largest lattice

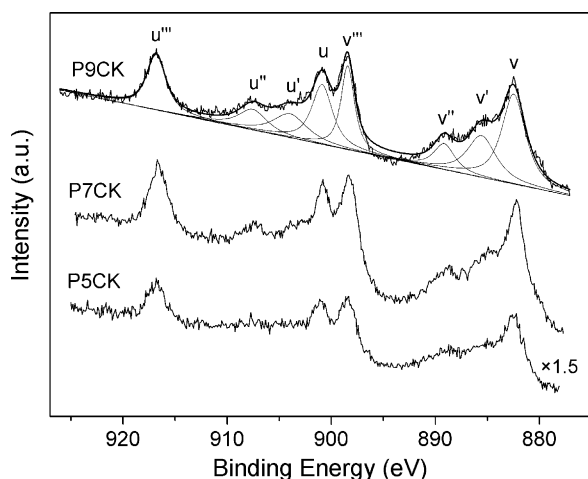


Fig. 4. Ce 3d spectra for the Pt-loaded catalysts.

parameter of P9CK, it can be deduced that the encapsulated Pt species in inner sphere of mixed oxides can probably facilitate the creation of oxygen vacancies via interdiffusion/interaction at the metal/support interface. The  $\text{Ce}^{3+}$  and oxygen vacancies on the rarely promoted surface, however, are oxidized or refilled by gaseous oxygen during the thermal treatment. For P5CK, most Pt particles exist on the surface of mixed oxides and hereby maintain the surface relatively rich in  $\text{Ce}^{3+}$  or oxygen vacancies, whereas the bulk of support is hardly affected. Thus, it appears reasonable that the lattice parameters of P5CK and CK approximate to each other.

In addition, we tried to quantify the content of chlorine on the surface with the assistance of XPS, since it has been well established that chloride ions from the metal precursor show a negative effect on the chemisorption and redox behavior of the support. However, no signals of Cl species were detected on any of our catalysts. According to the investigation by Holmgren et al. [25], the chlorine content, estimated from the Pt/Cl ratio by XPS, is approximately proportional to the ceria surface area. In this work, the absence of chlorine suggests that almost entire chlorine species on ceria-based mixed oxides with a surface area around  $5 \text{ m}^2 \text{ g}^{-1}$  can be removed by calcination in oxidizing condition at  $500^\circ\text{C}$  and above.

### 3.3. HRTEM

To explore the structural evolution at atomic scale, studies by high-resolution transmission electron microscope (HRTEM) were performed on all the Pt-supported samples. The representative micrographs are shown in Fig. 5a, c and e. In

order to provide more detailed information of the interfacial microstructure, the observed images were locally amplified and are shown in Fig. 5b, d and f, respectively. DDPs obtained by means of FFTs (shown in the insets) were applied to identify the metal and oxides phases. Analyses of these and other micrographs (not shown) reveal that the particle size of metal increases with the rising calcination temperature (see dispersion and average size of Pt particles listed in Table 1).

Focusing on P5CK, Fig. 5a shows a well crystallized Pt particle with the maximum diameter of ca. 9 nm in the center of the image. The enlarged image in Fig. 5b presents a clear fringe of the metal particle, differentiating Pt from the support particles. The lattice disorder of the mixed oxides, marked with white arrows in Fig. 5b, is observed at the interface where the CK particle leans on top of the metal particle and introduces the contiguity with Pt. Such a rearrangement of atoms in the support lattice may symbolize the effect of metal-support interaction on the microstructure of mixed oxides, which to some extent behaves as the slight expansion of cationic lattice revealed by XRD.

The metal particles on P7CK, which are not easily distinguished from the CK mixed oxides, are shown in Fig. 5c. The metal/oxides interfaces appear to be inexplicit. Fig. 5d exhibits that the Pt particle has immersed into the surroundings of CK particles, which indicates a partial encapsulation of metal by mixed oxides and consequently accounts for the loss of the surface Pt content on P7CK. Meanwhile, it can be roughly identified that the metal/oxides interface involves several atomic layers of both metal and mixed oxides, implying the interdiffusion of the correlative phases. It is noteworthy that the disorderly arranged Pt and Ce/Zr atoms and distortion of lattice, marked by white arrows, are distributed densely along the interface. Since these crystal defects are directly related to the formation of  $\text{Ce}^{3+}$  and oxygen vacancies, this observation appears supportive to the XPS results, which claims more abundant  $\text{Ce}^{3+}$  on the surface of P7CK.

The maximum diameter of the Pt particle in Fig. 5e is larger than 15 nm, which represents the sintering of Pt particles after the calcination at  $900^\circ\text{C}$ , and the particle is partially encapsulated by support particles. Notice that such an encapsulation appears different from those reviewed in literature [39], where encapsulation of metal particles by ceria species was induced by reductive treatment at  $700^\circ\text{C}$ . During the reductive treatment, the migration of the reduced ceria to the top of the metal microcrystals, rather than the burial of the metal particles into the ceria bulk, is the most likely decoration mechanism [39]. In this work, however, the burial of Pt

Table 2  
Surface composition and oxidation state of Ce and Pt species derived from XPS analyses

| Sample | Surface composition (at.%) |       |       |       |       | Ce/Zr | $\text{Pt}^{2+} f_{2/7}$ in Pt (%) | $\text{Ce}^{3+} 3d_{5/2}$ in Ce (%) |
|--------|----------------------------|-------|-------|-------|-------|-------|------------------------------------|-------------------------------------|
|        | Ce 3d                      | Zr 3d | La 3d | Pt 4f | O 1s  |       |                                    |                                     |
| P5CK   | 8.39                       | 6.66  | 1.88  | 3.09  | 79.98 | 1.3   | 100                                | 26.8                                |
| P7CK   | 11.64                      | 9.12  | 1.17  | 0.50  | 78.57 | 1.3   | 83.0                               | 30.2                                |
| P9CK   | 9.64                       | 9.94  | 1.67  | 0     | 78.75 | 1.0   | 0                                  | 23.9                                |

crystallites by support particles appears to be the potential mechanism. As revealed by Fig. 5e, several CK particles are located on top of a single Pt particle, and the metal particle is large enough to form interface with these support particles simultaneously. The enshrouding of Pt by the mixed oxides may also explain the signal absence of surface Pt species on P9CK examined by the XPS technology. The amplification of the metal/oxides interface reveals that, as shown in Fig. 5f, the 900 °C calcination induces a decreasing amount of the disorderly located atoms for both metal and mixed oxides, meaning improved crystallization and decreasing concentration of Ce<sup>3+</sup> or oxygen vacancies on the surface. Furthermore, it is worth noting that the integrally crystallized metal and mixed oxides show a semi-coherent atomic structure with the misfit dislocation (marked by white arrow) at the metal/oxides interface. It needs further investigations whether such a structure implies the formation of Pt–Ce alloys or Pt–CeO<sub>2</sub>–ZrO<sub>2</sub>–La<sub>2</sub>O<sub>3</sub> solid solution at even higher temperature.

### 3.4. TPR studies

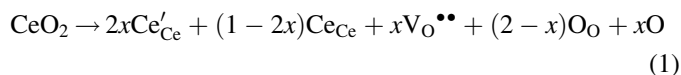
The reducibility of CK mixed oxides and Pt-supported catalysts was qualitatively characterized by TCD analysis and the TPR profiles are illustrated in Fig. 6. The reduction bands of surface and bulk oxygen of CK are to some extent overlapped and the maximum appears at ca. 580 °C, which corresponds well with the published observation in [40]. For P5CK, the promotion effect of Pt does not seem to play a key part in the reductive reaction because the release of bulk oxygen in the support does not appear dominant until the temperature increases up to ca. 560 °C. The tiny peak at ca. 210 °C represents the reduction of PtO and metal promoted ceria species [38,41,42] while the poorly identified peak at ca. 420 °C is assigned to the surface reduction of unpromoted support [40]. In the case of P7CK, the peaks at ca. 250 °C are ascribed to the reduction of Ce<sup>4+</sup> and Pt<sup>2+</sup> species with the main contribution from ceria. No other evident peaks at higher temperature were recorded. Combined with the discussion above, the role of metal/oxides interface on the reducibility of the support is highlighted. The larger surface content of Ce<sup>3+</sup> detected by XPS and the interfacial crystal defects observed by HRTEM both account for the upgraded reducibility of the catalyst. Dramatically, the profile of P9CK appears similar to that of bare CK support with two overlapped consumption bands at ca. 540 °C. This observation strongly supports our conjecture on encapsulation of Pt by support after the thermal ageing. The isolation of Pt species from the probe gas by mixed oxides may result in the disappearance of PtO reduction peak at low temperature. Compared with CK, the appreciably decreased reduction temperature and intensified peak for P9CK indicate that the encapsulated Pt particles are still available for the facilitation of creating oxygen vacancies in the mixed oxides.

### 3.5. OSC properties

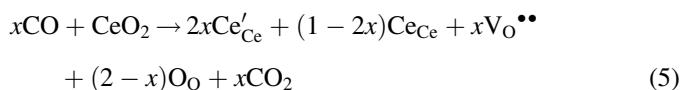
Dynamic oxygen storage capacity (DOSC) and oxygen storage capacity complete (OSCC) are regarded as two of the

most important parameters to evaluate the applicability of catalysts to rapidly switching lean/rich conditions. The DOSC values of catalysts at different temperatures are presented in Fig. 7. Since the thermodynamic and kinetic laws determine the mobility of bulk oxygen, the DOSC of all samples increase with the rise of testing temperature. Severe sintering results in the deteriorated oxygen release activity of CK support while the participation of Pt remarkably improves the dynamic OSC performance. According to Sugiura [10], the oxidation of CeO<sub>2</sub>–ZrO<sub>2</sub> mixed oxides, both with and without Pt, are faster than the reduction of support, and Pt has little effect on the oxides with respect to their uptake of oxygen. Therefore, the dynamic OSC is mainly determined by the oxygen release behavior of the support.

At the temperature as low as 200 °C, no conversion of CO to CO<sub>2</sub> was observed on any sample despite the consumption of H<sub>2</sub> over P5CK and P7CK in TPR tests. This observation reveals that the oxidation mechanisms of H<sub>2</sub> and CO on the supported catalysts are quite different. It is well known that the oxidation of H<sub>2</sub> on the precious metal catalysts relies heavily on the spillover effect, which splits H<sub>2</sub> molecules into H atoms by precious metal. These highly reactive H atoms can easily reduce oxides by donating electrons at relatively low temperature. On the other hand, the oxidation of CO are mainly oxidized on the surface of precious metal particles instead of on the support surface, and partial oxygen species that participate in the reactions are transferred from support to metal via a so-called back-spillover effect [16,43,44]. Hence, the oxidation of CO on the metal surface following Eley–Rideal mechanism [16] can be presented as follows:



where Eq. (1) expresses the formation of oxygen vacancies and Ce'<sub>Ce</sub> stands for the formation of Ce<sup>3+</sup>, Eq. (2) represents the chemisorption of active oxygen via back-spillover effect and \* stands for the Pt site, Eq. (3) means the formation of CO<sub>2</sub> on the metal surface and Eq. (4) the desorption of CO<sub>2</sub>. In the case of CK, i.e. direct interaction of CO with oxygen released by mixed oxides, the oxidation process can be expressed as:



In the case at 200 °C, the zero-production of CO<sub>2</sub> over all samples indicates that the low-surface-area mixed oxides could hardly supply any active oxygen by generating oxygen vacancies.

The little yields of CO<sub>2</sub> over CK at 300 °C imply that the direct interaction between CO and active oxygen species on the low-surface-area support barely occurs at this relatively low

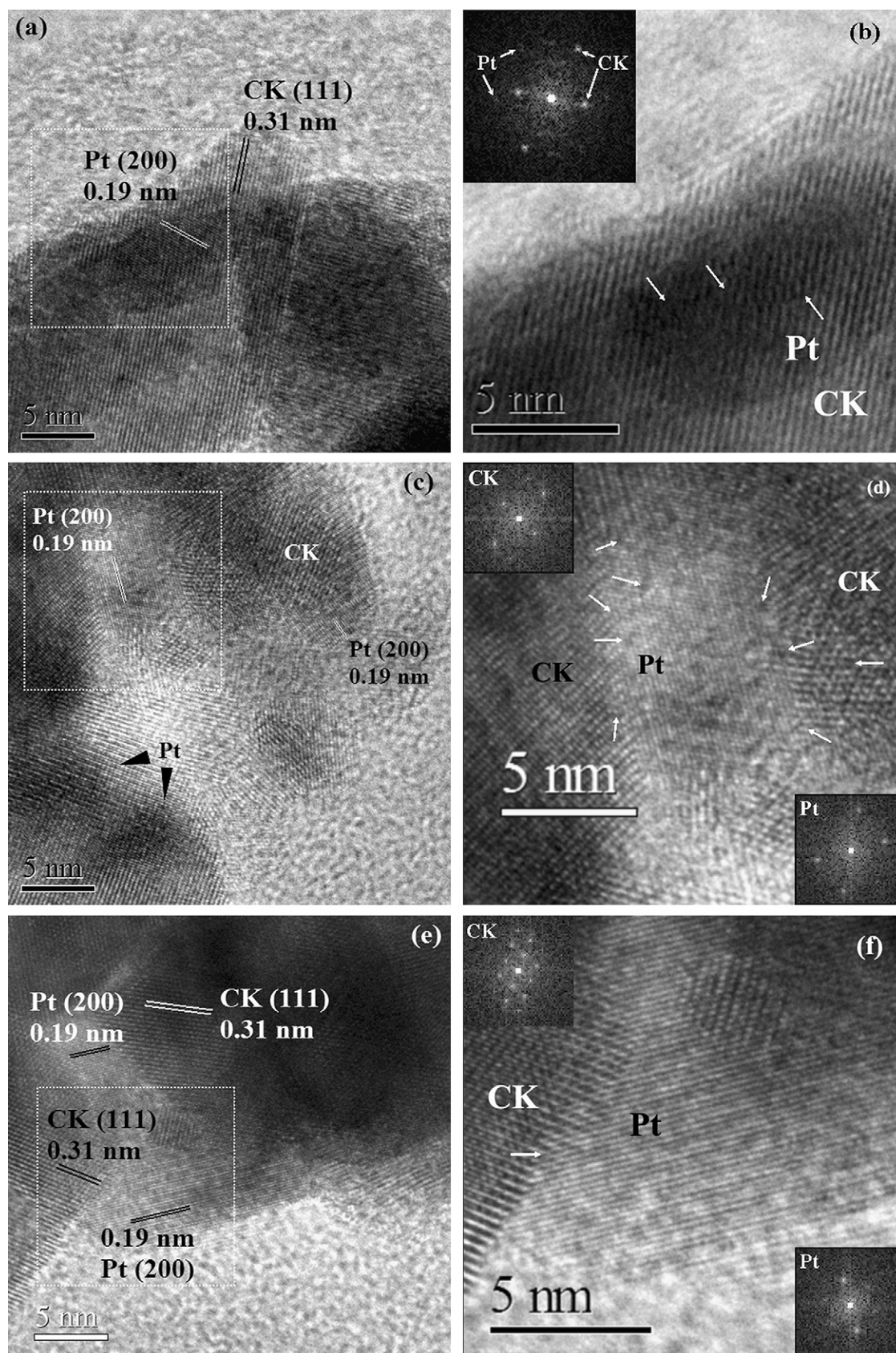


Fig. 5. Representative HRTEM micrographs of (a) P5CK, (c) P7CK and (e) P9CK with the amplifications of the dotted-line marked regions presented in (b), (d) and (f), respectively. Insets are the DDPs corresponding to an individual particle of Pt and CK in the selected regions.



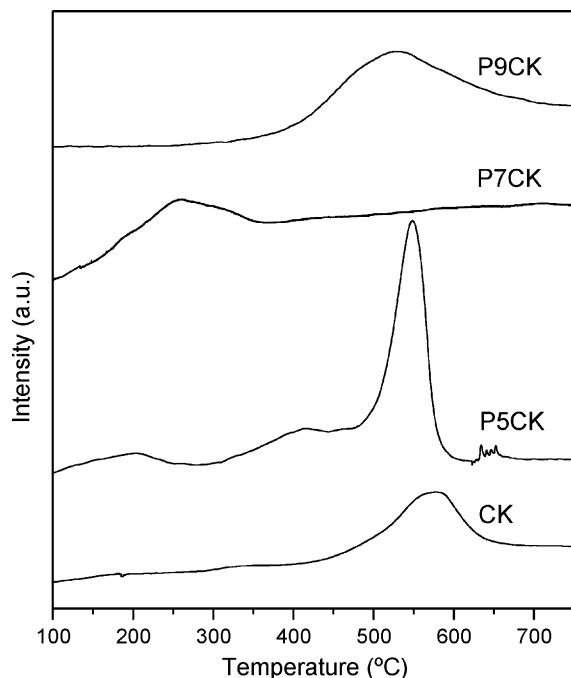


Fig. 6. TPR profiles of CK support and Pt-loaded catalysts.

temperature. Only on the surface of P5CK can the oxidation of CO initiates at this temperature. In order to separate the contribution of metal oxides to the OSC from that of the mixed oxides, the theoretical OSC supplied by metal oxides is estimated. The theoretical maximum contribution of PtO to the DOSC value is able to reach as high as  $102.6 \mu\text{mol CO}_2 \text{ g}^{-1}$ , assuming that all Pt atoms are distributed on the surface of the support and can be totally oxidized to  $\text{Pt}^{2+}$  and reduced to  $\text{Pt}^0$  in the transient condition. However, in practical situation, the atomic layers in the bulk of Pt particles are hardly affected by the redox cycle [23]. Based on the definition of dispersion and the assumption that only the top layer of the particles participated in the redox reaction and no Pt atoms were encapsulated by the support in P5CK, the theoretical OSC supplied by platinum oxides could be tentatively calculated from metal dispersion multiplied by the theoretical maximum contribution, resulting in the value of  $23.6 \mu\text{mol CO}_2 \text{ g}^{-1}$ . The rest OSC of P5CK at 300 °C, i.e.  $50.6 \mu\text{mol CO}_2 \text{ g}^{-1}$ , was mainly attributed to the contribution of mixed oxides promoted by Pt. As listed in Tables 1 and 2, the dispersions of Pt on P7CK and P9CK are smaller than that on P5CK, which indicates a possibility that less Pt atoms on P7CK and P9CK are affected by the transient conditions. At the meantime, the content of detectable Pt species on the surface of P7CK is much lower than that on P5CK, and even no Pt element was detected by XPS for P9CK, leading to a vast decline of chemisorption sites. These observations reasonably explain the rather limited contribution of PtO reduction to the DOSC of P7CK and P9CK. Meanwhile, the low chemisorption capability may also limit the reaction in Eq. (3) and the oxygen back-spilled from mixed oxides could not effectively contribute to the production of  $\text{CO}_2$ . As a result, very small OSC values were obtained over P7CK and P9CK at 300 °C.

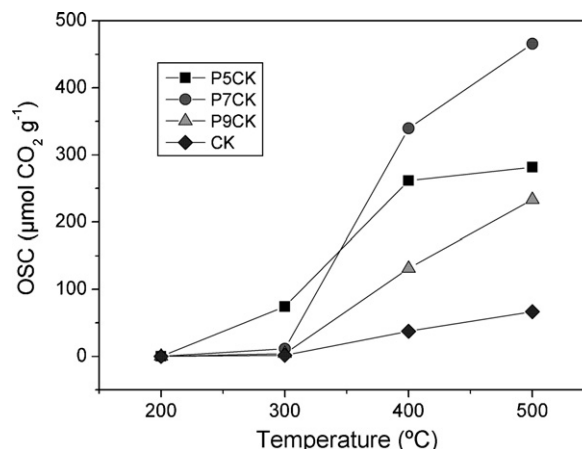


Fig. 7. Dynamic OSC values obtained from the production of  $\text{CO}_2$  at different temperatures.

At the range of 400–500 °C, the DOSC follows the sequence of  $\text{P7CK} > \text{P5CK} > \text{P9CK} > \text{CK}$ . If we assume the consumption of CO via the route in Eq. (5) is the same for different Pt-supported catalysts, the promotion effect of Pt on the oxygen release behavior of the CK support can be evaluated with the sequence of  $\text{P7CK} > \text{P5CK} > \text{P9CK}$  at 400–500 °C. It is worth noting that P7CK possesses neither the largest surface content of Pt nor the highest dispersion of metal. Therefore, the amount of chemisorption sites on Pt particles, which relies heavily on the surface content of Pt and metal dispersion, seems not to be essentially responsible for the enhancement of DOSC in this temperature range. Again, the encapsulation of Pt, which gestates the cationic sublattice disorder and other crystal defects in vicinity of metal/oxides interface and hereby facilitates the formation of  $\text{Ce}^{3+}$  or oxygen vacancies, should receive recognition for the outstanding DOSC of P7CK.

Fig. 8 presents the amounts of OSCC and labile oxygen (LOSC) derived from successive CO pulse test at 500 °C. The sums of the 10 OSC values for each sample are defined as the OSCC values, i.e. 77.0, 341.1, 512.6 and  $253.8 \mu\text{mol CO}_2 \text{ g}^{-1}$  for CK, P5CK, P7CK and P9CK, respectively. Agreeing well with the TPR and DOSC results, P7CK shows the most outstanding reducibility in this testing condition. One should note that, specifically for Pt-supported catalysts, the oxidation of CO by PtO is also taken into account in the testing procedure. With the hypothesis that the contribution of PtO to OSCC was in direct ratio to surface Pt content detected by XPS and this value for P5CK would be  $23.6 \mu\text{mol CO}_2 \text{ g}^{-1}$  as reported above, the amount of oxygen species from PtO on P7CK and P9CK can be figured as 3.8 and  $0 \mu\text{mol CO}_2 \text{ g}^{-1}$ , respectively. Thus, the modified OSCC values attributed to the support are 317.5, 508.8 and  $253.8 \mu\text{mol CO}_2 \text{ g}^{-1}$  for P5CK, P7CK and P9CK, respectively. Accordingly, the reduction ratios of  $\text{Ce}^{3+}/\text{Ce}$  after the test are estimated as 3.7%, 15.3%, 24.7% and 12.3% for CK, P5CK, P7CK and P9CK, respectively. It highlights the promotion effect of precious metal on the mobility of oxygen in low-surface-area ceria-based mixed oxides.

The value of LOSC, which deals with the  $\text{CO}_2$  production in the first CO pulse only, actually reflects the rate of oxygen

release. Again, the oxygen from metal oxide should be deducted when estimating the amount of oxygen released from oxides support. By using the same hypothesis proposed above, the labile oxygen species from mixed oxides are modified to 202.7, 378.1 and 116.2  $\mu\text{mol CO}_2 \text{ g}^{-1}$  for P5CK, P7CK and P9CK, respectively. Associated with the modified OSC concerning only mixed oxides, it can be deduced that ca. 14%, 64%, 74% and 46% of total available oxygen in the oxides are released during the first CO pulse for CK, P5CK, P7CK and P9CK, respectively. These data actually reveal that oxygen releasing rates follow the sequence of P7CK > P5CK > P9CK > CK as well. According to the literature [45], a  $\text{Ce}_{0.68}\text{Zr}_{0.32}\text{O}_2$  solid solution has a theoretical OSC of 3.8  $\mu\text{mol "O"} \text{ m}^{-2}$  assuming that there is no surface segregation of the  $\text{Ce}^{4+}$  and  $\text{Zr}^{4+}$  cations and an equal distribution of the (1 0 0), (1 1 0), and (1 1 1) planes. Meanwhile, it is noted that the theoretical number of surface oxygen atoms (atoms-O  $\text{nm}^{-2}$ ) differ by no more than 1.5% in the case of  $\text{Ce}_x\text{Zr}_{1-x}\text{O}_2$  ( $x > 0.5$ ) in either cubic or tetragonal crystal structures. It allows us take the same value of 3.8  $\mu\text{mol CO}_2 \text{ m}^{-2}$  for our CK mixed oxides of a similar composition. Hereby, the theoretical OSC supplied by monolayer of mixed oxides is 16.3  $\mu\text{mol CO}_2 \text{ g}^{-1}$  given the BET surface area of CK support. Then it can be deduced that oxygen atoms from approximately 5, 13, 18 and 6 surface and subsurface layers are activated and driven to the reaction in the first CO pulse for CK, P5CK, P7CK and P9CK, respectively. Since such numbers of atomic layers still concern the surface and subsurface status of support, the correlation between the XPS results and oxygen releasing rate can be constructed. The sequences, arranging the amount of labile oxygen and the rate of oxygen release, accord with that of the percentage of  $\text{Ce}^{3+}$  in Ce species for the Pt-supported catalysts. This accordance confirms that the abundance of  $\text{Ce}^{3+}$  or oxygen vacancies facilitates the transfer and release of oxygen atoms from the mixed oxides [13]. Bringing together the discussion on the thermal ageing of Pt on mixed oxides, it can be deduced that the partial encapsulation of metal by support is beneficial to increasing both the amount of active oxygen and the oxygen releasing rate though a loss of chemisorption sites on the metal surface is taken into consideration in this case.

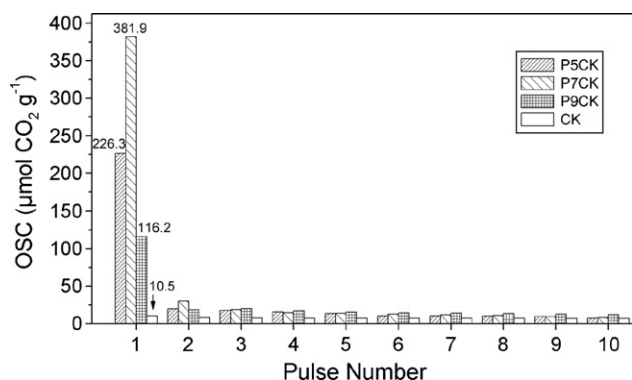


Fig. 8. Amount of labile oxygen (LOSC) and OSC value calculated from  $\text{CO}_2$  production in each CO pulse.

In addition, focusing on the third to tenth CO pulse, one can see that the largest amount of released oxygen during each pulse was supplied by P9CK. Since these oxygen species are purely originated from the very inner layers of the support, it approves our earlier deduction that encapsulated Pt species are capable to facilitate the creation of oxygen vacancies in the bulk of mixed oxides.

#### 4. Conclusions

The oxidizing thermal treatment at the temperature of 700 °C and above induces not only the sintering of Pt particles but also the encapsulation of Pt by low-surface-area  $\text{CeO}_2$ – $\text{ZrO}_2$ – $\text{La}_2\text{O}_3$  mixed oxides. The potential mechanism of such an encapsulation is figured as the burial of metal by support particles. The distortion of the support lattice and other crystal defects, indicating the interdiffusion/interaction between the metal and mixed oxide, was observed at the metal/oxides interface by HRTEM. The OSC results show that the status of metal/oxides interface is particularly relevant to the reducibility and oxygen release behavior of the low-surface-area mixed oxides. By creating crystal imperfections along the metal/oxide interface, encapsulation of Pt elevates the abundance of  $\text{Ce}^{3+}$  and oxygen vacancies not only on the surface but also in the bulk of oxides, and hereby increases the amount of labile oxygen as well as the rate of oxygen release.

#### Acknowledgements

The authors would like to acknowledge the Ministry of Science and Technology, PR China for the financial support of Project 2004CB719503, 2006AA060305 and National Natural Science Foundation of China for the financial support of Project 50502023. Moreover, we would also thank the Center of Analysis and Key Lab of Advanced Materials in Tsinghua University.

#### References

- [1] M. Shelef, R.W. McCabe, *Catal. Today* 62 (2000) 35.
- [2] H.S. Gandhi, G.W. Graham, R.W. McCabe, *J. Catal.* 216 (2003) 433.
- [3] J. Kašpar, P. Fornasiero, N. Hickey, *Catal. Today* 77 (2003) 419.
- [4] S. Matsumoto, *Catal. Today* 90 (2004) 183.
- [5] H. Shinjoh, *J. Alloys Comp.* 408–412 (2006) 1061.
- [6] J.P. Cuif, G. Blanchard, O. Touret, A. Seigneurin, M. Marczi, E. Quémeré, *SAE Paper* 970463 (1997).
- [7] M. Yashima, H. Arashi, M. Kakihana, M. Yoshimura, *J. Am. Ceram. Soc.* 77 (1994) 1067.
- [8] R. Si, Y. Zhang, S. Li, B. Lin, C. Yan, *J. Phys. Chem. B* 108 (2004) 12481.
- [9] K. Minami, T. Masui, N. Imanaka, L. Daib, B. Pacaud, *J. Alloys Compd.* 408–412 (2006) 1132.
- [10] M. Sugiura, *Catal. Surv. Asia* 7 (2003) 77.
- [11] Y. Nagai, T. Yamamoto, T. Tanaka, S. Yoshida, T. Nonaka, T. Okamoto, A. Suda, M. Sugiura, *Catal. Today* 74 (2002) 225.
- [12] C.E. Hori, A. Brennera, K.Y.S. Ng, K.M. Rahmoeller, David Belton, *Catal. Today* 50 (1999) 299.
- [13] C. Bozo, N. Guilhaume, J.-M. Herrmann, *J. Catal.* 203 (2001) 393.
- [14] G.E. Arena, G. Centia, G. Deganello, L.F. Liotta, A. Macaluso, G. Pantaleo, *Top. Catal.* 30/31 (2004) 397.

- [15] A. Galdikas, C. Descorme, D. Duprez, F. Dong, H. Shinjoh, *Top. Catal.* 30/31 (2004) 405.
- [16] C.N. Costa, S.Y. Christou, G. Georgiou, A.M. Efstathiou, *J. Catal.* 219 (2003) 259.
- [17] H. Birgersson, L. Eriksson, M. Boutonnet, S.G. Järås, *Appl. Catal. B: Environ.* 54 (2004) 193.
- [18] X. Wang, R.J. Gorte, J.P. Wagner, *J. Catal.* 212 (2002) 225.
- [19] P.J.F. Harris, *J. Catal.* 97 (1986) 527.
- [20] R.M.J. Fiedorow, B.S. Chahar, S.E. Wanke, *J. Catal.* 51 (1978) 193.
- [21] Y. Nagai, T. Hirabayashi, K. Dohmae, N. Takagi, T. Minami, H. Shinjoh, S. Matsumoto, *J. Catal.* 242 (2006) 103.
- [22] G.W. Graham, H.-W. Jen, W. Chun, R.W. McCabe, *Catal. Lett.* 44 (1997) 185.
- [23] G.W. Graham, H.-W. Jen, W. Chun, R.W. McCabe, *J. Catal.* 182 (1999) 228.
- [24] A. Trovarelli, *Catalysis by Ceria and Related Materials*, vol. 2, Imperial College Press, London, 2001.
- [25] A. Holmgren, F. Azamouh, E. Fridell, *Appl. Catal. B: Environ.* 22 (1999) 49.
- [26] J.E. Beson, M. Boudart, *J. Catal.* 4 (1965) 704.
- [27] H.C. Yao, Y.F. Yu Yao, *J. Catal.* 86 (1984) 254.
- [28] F.C. Galisteo, R. Mariscal, M.L. Granados, J.L.G. Fierro, R.A. Daley, J.A. Anderson, *Appl. Catal. B: Environ.* 59 (2005) 227.
- [29] G.W. Graham, A.N. Shigapov, *Catal. Lett.* 81 (2002) 253.
- [30] X. Wu, J. Fan, R. Ran, D. Weng, *Chem. Eng. J.* 109 (2005) 133.
- [31] C. Larese, M.L. Granados, R. Mariscal, J.L.G. Fierro, P.S. Lambrou, A.M. Efstathiou, *Appl. Catal. B: Environ.* 59 (2005) 13.
- [32] B.M. Reddy, A. Khan, P. Lakshmanan, M. Aouine, S. Loridant, J.-C. Volta, *J. Phys. Chem. B* 109 (2005) 3355.
- [33] B.M. Reddy, A. Khan, *Catal. Surv. Asia* 9 (2005) 155.
- [34] Y. An, M. Shen, J. Wang, *J. Alloys Compd.* 441 (2006) 305.
- [35] H. Vidal, J. Kašpar, M. Pijolat, G. Colon, S. Bernal, A. Córdón, V. Perrichon, F. Fally, *Appl. Catal. B: Environ.* 27 (2000) 49.
- [36] O. Stonehart, *J. Appl. Electrochem.* 112 (1992) 9952105.
- [37] G.W. Graham, H.-W. Jen, R.W. McCabe, A.M. Straccia, L.P. Haack, *Catal. Lett.* 67 (2000) 99.
- [38] J. Fan, X. Wu, R. Ran, D. Weng, *Appl. Surf. Sci.* 245 (2005) 162.
- [39] S. Bernal, J.J. Calvino, M.A. Cauqui, J.M. Gatica, C. Larese, J.A. Pérez Omil, J.M. Pintado, *Catal. Today* 50 (1999) 175.
- [40] F. Fally, V. Perrichon, H. Vidal, *Catal. Today* 59 (2000) 373.
- [41] L.V. Mattos, E.R. de Oliveira, P.D. Resende, *Catal. Today* 77 (2002) 245.
- [42] F.B. Passos, E.R. de Oliveira, L.V. Mattos, *Catal. Today* 101 (2005) 23.
- [43] P.S. Lambrou, A.M. Efstathiou, *J. Catal.* 240 (2006) 182.
- [44] S.Y. Christou, C.N. Costa, A.M. Efstathiou, *Top. Catal.* 30/31 (2004) 325.
- [45] Y. Madier, C. Descorme, A.M. Le Govic, D. Duprez, *J. Phys. Chem. B* 103 (1999) 10999.